ADVANCED MATERIALS
www.advmat.de

Toward Plasmonic Neural Probes: SERS Detection of Neurotransmitters through Gold-Nanoislands-Decorated Tapered Optical Fibers with Sub-10 nm Gaps

Di Zheng, Filippo Pisano, Liam Collard, Antonio Balena, Marco Pisanello, Barbara Spagnolo, Rosa Mach-Batlle, Francesco Tantussi, Luigi Carbone, Francesco De Angelis, Manuel Valiente, Liset M. de la Prida, Cristian Ciracì, Massimo De Vittorio,* and Ferruccio Pisanello**

Integration of plasmonic nanostructures with fiber-optics-based neural probes enables label-free detection of molecular fingerprints via surface-enhanced Raman spectroscopy (SERS), and it represents a fascinating technological horizon to investigate brain function. However, developing neuroplasmonic probes that can interface with deep brain regions with minimal invasiveness while providing the sensitivity to detect biomolecular signatures in a physiological environment is challenging, in particular because the same waveguide must be employed for both delivering excitation light and collecting the resulting scattered photons. Here, a SERS-active neural probe based on a tapered optical fiber (TF) decorated with gold nanoislands (NIs) that can detect neurotransmitters down to the micromolar range is presented. To do this, a novel, nonplanar repeated dewetting technique to fabricate gold NIs with sub-10 nm gaps, uniformly distributed on the wide (square millimeter scale in surface area), highly curved surface of TF is developed. It is experimentally and numerically shown that the amplified broadband near-field enhancement of the high-density NIs layer allows for achieving a limit of detection in aqueous solution of 10^{-7} M for rhodamine 6G and 10^{-5} M for serotonin and dopamine through SERS at near-infrared wavelengths. The NIs-TF technology is envisioned as a first step toward the unexplored frontier of in vivo label-free plasmonic neural interfaces.

1. Introduction

As the field of optogenetics has stimulated the development of optical neural interfaces to deliver light into the brain,[1–6] the advent of genetically encoded fluorescent indicators (GEI) of neural activity has enabled cell-type-specific monitoring of chemical compounds, including Ca^{2+}[7–9] and several types of neurotransmitters including glutamate,[10–13] γ-aminobutyric acid (GABA),[14] serotonin,[15] dopamine,[16,17] acetylcholine[18] and norepinephrine.[19] These reporters have achieved considerable success in unveiling neurotransmitter dynamics, at synaptic resolution,[20,21] and with neural probe devices.[22–25] However, the use of exogenous reporters is still an indirect way to investigate biological systems, which adds extra complexity or even alters the native state of the system.[26,27] Thus, the neuroscience field would highly benefit from label-free approaches to optically probe neurotransmitter dynamics.[28,29]

D. Zheng, F. Pisano, L. Collard, A. Balena, M. Pisanello, B. Spagnolo, R. Mach-Batlle, C. Ciracì, M. De Vittorio, F. Pisanello
Istituto Italiano di Tecnologia
Center for Biomolecular Nanotechnologies
Arnesano, LE 73010, Italy
E-mail: di.zheng@iit.it; massimo.devittorio@iit.it; ferruccio.pisanello@iit.it

F. Tantussi, F. De Angelis
Istituto Italiano di Tecnologia
Center for Convergent Technologies
Genova 16163, Italy

L. Carbone
CNR NANOTEC - Institute of Nanotechnology
University of Salento
Lecce 73100, Italy

M. Valiente
Brain Metastasis Group
Spanish National Cancer Research Center (CNIO)
Madrid 28029, Spain

L. M. de la Prida
Instituto Cajal
CSIC
Madrid 28002, Spain

M. De Vittorio
Dipartimento di Ingegneria Dell'Innovazione
Università del Salento
Lecce 73100, Italy

The ORCID identification number(s) for the author(s) of this article can be found under https://doi.org/10.1002/adma.202200902.

DOI: 10.1002/adma.202200902

To do this, surface-enhanced Raman spectroscopy (SERS) represents a promising method for ultrasensitive, label-free detection down to single-molecule level.[30–32] However, bringing SERS into the brain represents a challenge from the substrate point of view, and the most convenient approach is using plasmonic-enhanced optical fibers. Optical-fiber-based neural probes are indeed widely employed to optically access brain tissue, and they have been extensively used to reveal neural activity by collecting fluorescence of GEI in a fiber photometry configuration.[22–25,33,34] Among these, tapered optical fibers (TFs) are particularly attractive to develop this technology for two reasons: i) the tapered shape can minimize the damage to the tissue, enabling extensive use in vivo;[35–37] and ii) the photonic properties of the taper give access to mode-division de-multiplexing strategies to deliver and collect light over a large optically active area on the square millimeter scale.[38] Therefore, integrating TFs with plasmonic structures represents an important path to explore a novel generation of neural implants for studying chemical signalling in the brain.

In this framework, an optimized plasmonic TF probe for SERS would need to simultaneously: i) enhance excitation yield, with high density hotspots distributed across a wide taper surface, ideally operating with a wide range of polarization directions and wavevector components (including the evanescent ones) supported by the fiber; ii) efficiently collect scattered signal, providing the highest possible overlap between a hotspot-confined electromagnetic field and modal functions of guided modes; and iii) hold plasmonic resonances covering both excitation and scattered wavelengths in the NIR to reduce the influence of tissue fluorescence background.

Possible fabrication strategies to achieve this aim include top-down and bottom-up approaches, and our group recently demonstrated the integration of cellular-sized curved plasmonic structures on a TF to engineer the spectral and angular patterns of optical emission and collection,[39] using focused ion beam milling at low fluences.[40] However, scaling this top-down approach will intrinsically result in unmanageable fabrication times when large surface area sensitivity is required. High-throughput bottom-up strategies (such as deposition of colloidal nanoparticles, direct synthesis, and electrostatic self-assembly) have been reported to produce TFs decorated with plasmonic nanoparticles for SERS molecular sensing,[41–51] though the fabricated structures always result in either multilayer, uneven cluster assembly, wide interparticle separation (tens of nanometers) or particles located far away from the dielectric surface (tens of nanometers). Indeed, the deposition of colloidal gold nanoparticles method has been used to realize SERS nanosensors, and the enhanced neurotransmitters' Raman signal close to cultured neurons were demonstrated, but with light excitation and collection occurring from the outside of the device.[42,43] Furthermore, TFs coated with silver-doped poly(vinyl alcohol) (PVA) have been reported to detect dopamine SERS signal through the fiber but this was done at lower sensitivity (10^{-3} M) in the visible region.[49] Overall, none of them demonstrated the ability to achieve a neural probe combining the above mentioned features (i–iii). Therefore, an effective strategy of fabricating plasmonic neural probes able to deliver excitation light while collecting SERS signal of neurotransmitters at physiological levels remains a technological challenge, whose solution can pave the way toward the use of plasmonic devices for neuroscience applications.

Here, we implemented a nonplanar repeated dewetting (npRDW) technique to obtain uniformly distributed gold nanoislands (NIs) with inter-island gaps ≤10 nm, decorated along and around the highly curved surface of a TF neural probe. The narrowing of metallic gaps obtained via consecutive processes of dewetting redshifts the plasmonic resonance of the system, and thus improves SERS determination under 785 nm laser excitation with a limit of detection (LOD) of 10^{-7} M for R6G in aqueous solution over the wide sensitive surface of the taper. Strikingly, the dewetted gold NIs-TFs devices show a LOD of 10^{-5} M in the NIR region for neurotransmitters, including aqueous solutions of serotonin and dopamine, overcoming the current limits of other approaches employing excitation and collection fields guided in the same waveguide,[49] and is compatible with the upper bound level of concentrations for neurotransmitters, measured to be in the tens of micrometers range for both dopamine and serotonin.[15,16,52–54] On the strength of these results, we believe that the highly sensitive SERS detection of the NIs-TFs platform offers opportunities for further neural interfacing applications in monitoring neurotransmitters dynamics in vivo.

1.1. Nonplanar Repeated Dewetting for Plasmonic Tapered Optical Fibers

Figure 1a shows a schematic representation of the plasmonic TFs presented in this work, featuring highly packed gold NIs with <10 nm nanogaps on the nonplanar surface of the fiber taper. This is achieved by a npRDW method, with the fabrication steps depicted in Figure 1b. TFs were obtained by a heat-and-pull method from commercially available core/cladding step-index silica fibers (NA 0.22). The thinning of the waveguide gradually reduces the number of guided modes allowed by the waveguide, and lets guided radiation couple with photonic structures on the taper surface over a segment that can be tailored from a few hundred micrometers to a few millimeters.[55] As the fibers have been locally heated above the silica transition temperature of 1207 °C, the high temperature results in a clean and smooth TF surface before the evaporation. Thus, without the need for an additional cleaning step, a layer of gold with initial thickness t_1 = 5 nm is deposited on the curved surface of the taper with a rotational motor mount in the chamber of an e-beam evaporator, to ensure conformal gold evaporation over the entire TF surface. To obtain the first layer of NIs, thermal annealing is then performed by raising the temperature from room temperature to 600 °C with a rate of 10 °C min^{-1}, after which, the temperature is held at 600 °C for 1 h. This thermal treatment is performed in standard atmospheric conditions, which has been reported to increase the bond between gold to fused silica by promoting diffusion of Au into the silica, due to the presence of oxygen.[56,57] A nonplanar single dewetting (npSDW) procedure is completed after a cycle of rotational evaporation and dewetting process. The second cycle of gold deposition t_2 = 5 nm and thermal dewetting is conducted successively to generate denser plasmonic active NIs patterns with enhanced optical capability. The npRDW

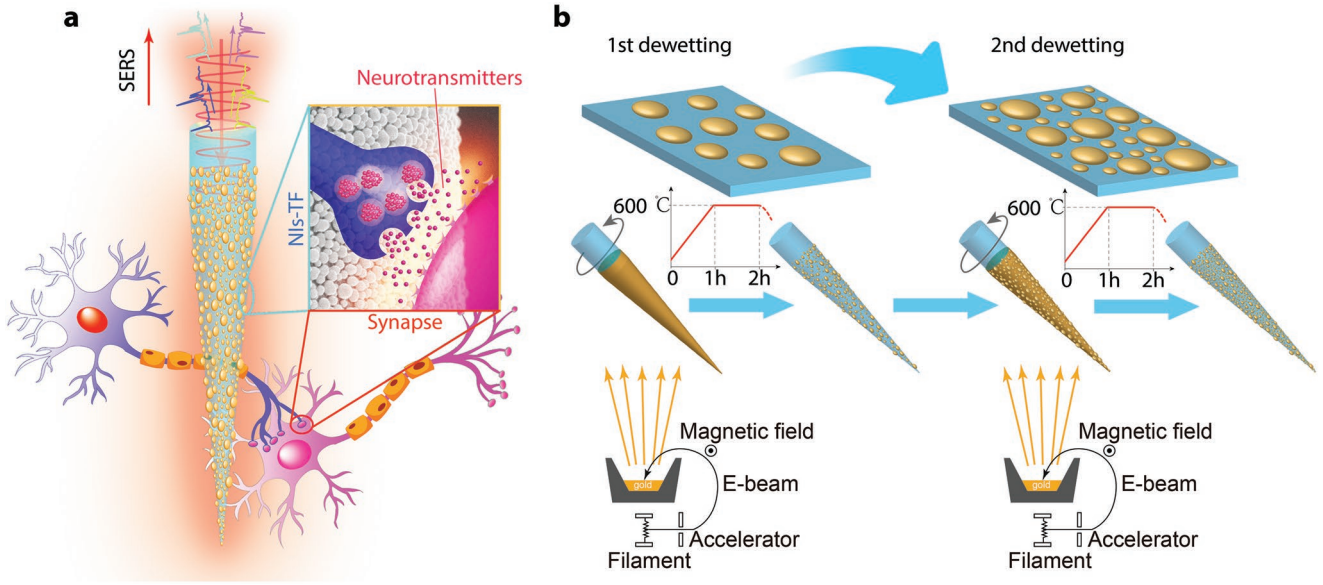

Figure 1. a) Schematic illustration of npRDW TFs for neurotransmitters' SERS signal detection. b) Schematic illustration of fabrication procedures of npRDW TFs.

procedure is completed after all the processes above, as schematically shown in Figure 1b (detailed fabrication parameters are reported in Experimental Section).

A representative fabrication output is reported in **Figure 2**. The optical images in Figure 2a show the overview of a noncoated (blank), 5 nm gold thin film covered, and NIs-covered

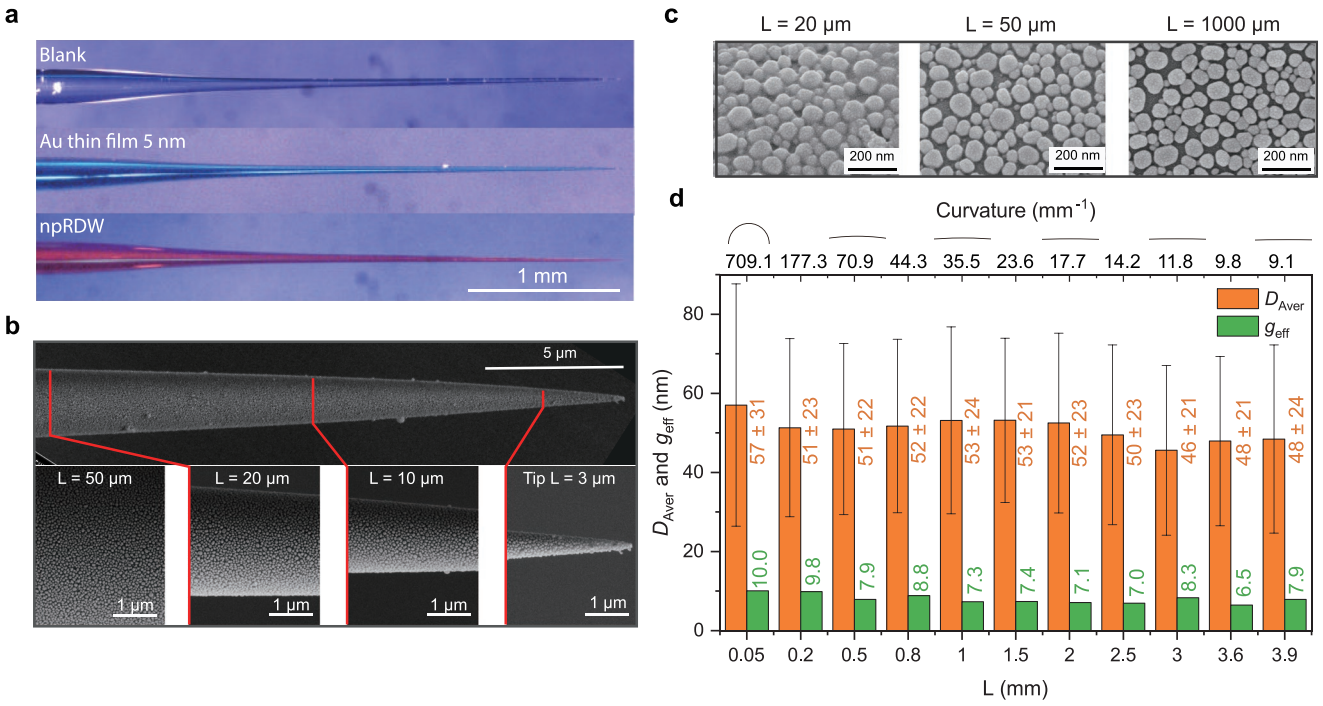

Figure 2. Morphology of TFs fabricated by npRDW. a) Optical images of noncoated (blank), 5 nm gold thin film covered, and npRDW TFs (from top to the bottom). b) SEM images showing the morphology at the very tip of a npRDW TF; the bottom images are the corresponding enlarged views of NIs on the taper (from left to right, images are taken at a distance away from tip $L = 50$, 20, 10 and 3 μm, at the section highlighted by the red lines). c) High-magnification SEM images used for the statistical analysis (from left to right, images are taken at $L = 20$, 50, and 1000 μm respectively). d) Statistical analysis for average NIs diameters (orange bars with the standard deviation as error bars) and effective gap size (green bars) distribution starting from $L = 50$ μm to the taper end of $L = 3.9$ mm, the short-curved markers on the top graphically show relative curved surface together with the curvature value.

TF fabricated by npRDW (taper length > 3.5 mm in all cases). As the uniform cover of gold plasmonic active NIs absorb the majority of the blue and green light, the whole body of NIs TF appears pink under direct illumination with broadband light, making a prominent difference from the blank and gold thin film covered TFs. SEM inspections (Figure 2b) indeed show a homogenous distribution of NIs along and around the taper, and the high-magnification images reveal that the NIs are evenly spread over the whole body of the TF until its very tip. To gain a quantitative picture of how NIs and inter-islands gaps distribute along the taper, high-magnification SEM images were taken through the entire narrowing region, and the distribution of NIs was analyzed as a function of the curvature of the waveguide. Figure 2c shows representative SEM images used for statistical analysis, with images taken from positions with a distance away from tip L = 20, 50 and 1000 µm (from left to right). Systematic and quantitative morphological analysis (see Experimental Section) displayed in the bar graph in Figure 2d shows that the average diameter (≈50 nm) and the effective gap (<10 nm) of NIs are uniform along the taper despite a large curvature difference between the very tip region and the taper end.

1.2. Enhanced Optical Properties from Repeated Dewetting

The two consecutive treatments of dewetting have proved effective to achieve very narrow gaps amongst NIs. More specifically, gold NIs formed during the first dewetting process operate themselves as sites for the further nucleation of gold originating from the second process of deposition/dewetting, thus enlarging their sizes; additionally, a contemporary side-nucleation forming new smaller NIs is also observed, resulting thereby in a bi-modal NIs size dispersion and more densely covered surface. This behavior is displayed on a flat silica substrate in **Figure 3**a. SEM images and the corresponding analysis of NIs' size distribution show the evolution from single Gaussian to bi-Gaussian size distribution from the first to second dewetting step, with a slightly reduced NIs' average diameter (from 51 to 46 nm) and prominently decreased effective gap size (from ≈30 to <10 nm, see bar graph in Figure 3b; details on statistical analysis are described in the Experimental Section). The corresponding extinction spectra reported in Figure 3c, show a direct dependance on the morphological properties. As the packing density increases from single dewetting (SDW) to repeated dewetting (RDW) samples, the enhanced interparticle

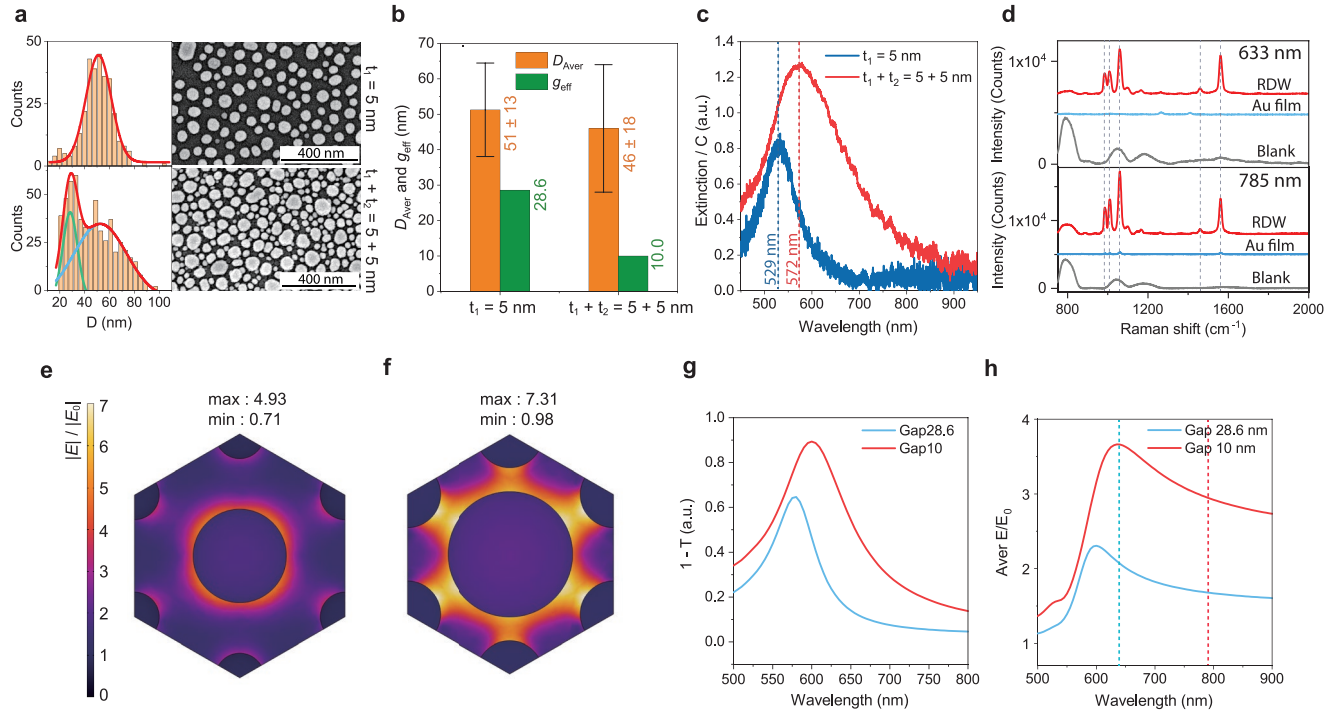

Figure 3. a) SEM morphologies and corresponding NIs diameter distribution of SDW t_1 = 5 nm (top) and RDW $t_1 + t_2$ = 5 + 5 nm (bottom), the left panels are the corresponding NIs distribution histogram with single Gaussian fitting centered at 51 nm for SDW and two Gaussian fittings centered at 53 and 28 nm, respectively, for RDW. b) Statistical analysis of average diameter (orange bars) with standard deviation as error bar and effective gap (green bars) of SDW and RDW morphologies shown in (a). c) The extinction spectra divided by corresponding coverage rates of SDW (blue line) and RDW (red line) samples. d) SERS measurements on flat substrates with 633 (top) and 785 nm (bottom) excitations, the curves within corresponding to bare (gray curve), 10 nm gold thin film (blue curve), and RDW NIs (red curve) substrates. The dashed vertical lines indicate the molecular signature peaks at 992, 1015, 1065, 1465, and 1567 cm^{-1}. e,f) Simulated near-field enhancement spatial map of hexagonal periodic model with 28.6 nm gap (e) and 10 nm gap (f) between the central disks and surrounding disks with the nonpolarized excitation at 633 nm (the diameter of central and surrounding gold disks are 53 and 28 nm, respectively, and the thickness of the disks is 15 nm). g) The broadband spectral response of hexagonal periodic gold disk models with 28.6 nm gap (blue line) and 10 nm gap (red line), respectively, reported with a coefficient (1 − T), where T is the transmittance of the system at normal incidence. h) Wavelength dependence for average near-field enhancement of periodic hexagonal model (blue and red curve correspond to the model with a gap size of 28.6 and 10 nm, respectively, and the blue and red dashed lines indicate the experimental excitation wavelengths at 633 and 785 nm, respectively).

interaction redshifts the resonance position (from 529 to 583 nm), broadens the full width at half maximum, from 87.5 to 206.7 nm because of increased randomness both from size and shape of NIs, and increases the extinction intensity.

The SERS response of the NIs' was characterized by comparing the RDW sample to 10 nm gold thin film covered and blank samples. All the samples went through the same functionalization procedures of benzenethiol (BT) molecules (Figure 3d), taking advantage of BT to systematically self-assemble onto gold surfaces through gold–sulfur bonds.[58,59] Although the resonance position for the RDW sample overlaps better with the 633 nm excitation line, SERS measurements on flat substrate show NIs operate efficiently at both 633 and 785 nm Raman excitation wavelengths (see Experimental Section for technical details and BT molecules functionalization procedures). SERS spectra from BT molecules exhibit enhancements over 50 and 20 (with respect to thin gold film samples), respectively, for the two wavelengths, showing the suitability of RDW NIs for applications requiring a broadband response.

To explain how this peculiar NIs distribution results in the plasmon resonance redshifting, the enhanced extinction and the broadband SERS response behaviors, we have built a simplified numerical model composed of a periodic hexagonal array of gold disks (see Experimental Section). This model allows us to isolate and appreciate the impact of the interparticle distances and to avoid otherwise computationally very demanding calculations. Simulated near-field enhancement spatial maps and transmission spectra for the SDW and RDW representative models are shown in Figure 3e–g, respectively. As expected from the experiments in Figure 3c, the increased interparticle interaction redshifts the resonance position, improves the near-field enhancement factor (Figure 3e,f) and decreases the transmission intensity, with the theoretical extinction reflecting the trend of the experimental measurements (Figure 3g). Interestingly, the narrowing of the gaps results in a nearly two-times increase of the average near-field enhancement factors. In addition, the hexagonal periodic model shows that the average near-field enhancement at 785 nm is 80% of the enhancement at 633 nm (Figure 3h). Such a strong tail in the enhancement function toward longer wavelength can be explained considering that gold interband transitions play a minor role in this spectral range. This explains the broadband SERS response observed in Figure 3d. The combination of the redshift and increased near-field enhancement resulting from the RDW shows that the RDW gold NIs provide enhanced SERS sensibility toward the NIR region, an important feature to reduce tissue autofluorescence background in biological applications.[60,61]

1.3. Through-TF SERS of Neurotransmitters in Solutions

To examine the detection capability of the fabricated npRDW TF device, through-TF SERS measurements are carried out with a custom Raman microscope operating at 785 nm wavelength continuous laser excitation, as schematically shown in **Figure 4**a (see Experimental Section for details). The SERS performance of NIs-TFs is examined using several molecules: BT, rhodamine 6G (R6G), serotonin, and dopamine.

First, BT molecules are functionalized on NIs-TFs to measure the resulting spectra collected by the TFs. Representative results are displayed in Figure 4b: the BT molecule signal (peaks at 992, 1015, 1065, 1465 and 1567 cm^{-1}) collected through the npRDW TF (red line) shows a clear enhancement compared with the control samples consisting respectively of a bare TF (gray line), a TF hosting a 10 nm-thick gold layer (black line), and a plasmonic TFs with NIs obtained with a single dewetting step (green line). The higher signal enhancement of the npRDW tapers is due to denser nanogaps and stronger near-field enhancement, as described in the previous section.

We then implement an experimental procedure to measure the LOD of npRDW TFs for molecules in aqueous solutions, using first the model dye R6G as a reference. The measurements start from the lowest concentration solution and increase toward the highest concentration in steps, using a single fiber for each concentration ramp. Each spectrum is taken immediately after the fiber tip was immersed entirely into the aqueous solution, and the fiber tip is kept in the solution during the entire exposure time (details are described in Experimental Section). Figure 4c shows the SERS spectra of R6G solution with concentrations varying from 10^{-10} to 10^{-4} M. The R6G signature peaks at 1356 and 1504 cm^{-1} are recognizable from the lowest concentration of 10^{-7} M. This is also reflected in the analysis of the integral of the peaks intensity after locally subtracting the background (shown in the inset) which shows a rising point at 10^{-7} M as npRDW TFs LOD for R6G. Upon increasing the concentrations, more molecular signature peaks gradually appear, including 1304, 1569 and 1643 cm^{-1}. The LOD is observed at 10^{-4} M for the blank TF control experiment (see Figure S1, Supporting Information).

Having established the approach, the LOD of the npRDW TFs is then characterized for serotonin and dopamine aqueous solutions. Figure 4d shows a set of spectra taken from serotonin aqueous solution with concentrations varying from 10^{-8} to 10^{-4} M. The serotonin signature peaks (1335 and 1535 cm^{-1}) start to appear from a concentration of 10^{-5} M, along with a rising point in the slope of the integral intensities versus concentration (Figure 4d, inset), which marks the LOD of 10^{-5} M for serotonin aqueous solution. The SERS signal collected for dopamine, displays in Figure 4e, shows instead an overall intensity increase in the region from 1400 to 1734 cm^{-1}, with the strongest peak at 1476 cm^{-1} distinguishable from a concentration as low as 10^{-5} M. To further identify the molecular features in the overlapped spectra, all the original spectra in Figure 4e are subtracted by zero concentration spectra (fiber in water), as shown in Figure 4f. The dopamine signature peaks at 1476 cm^{-1}, along with more peaks (1268 and 1323 cm^{-1}) become clearly distinguishable from a concentration of 10^{-5} M, which marks the LOD for dopamine case. The subtracted background is to be mainly ascribed to the silica Raman spectrum of the waveguide, as it is employed for both excitation and collection. The Raman response of the waveguide material indeed overlaps with or even submerges the SERS molecular fingerprints. The ability to identify molecule-specific spectral features depends on the relative strength of the two signals (i.e., molecular SERS versus silica Raman). Among all the molecules tested herein, we have observed that the relative strength of molecular SERS gradually decreases from BT to R6G, to neurotransmitters

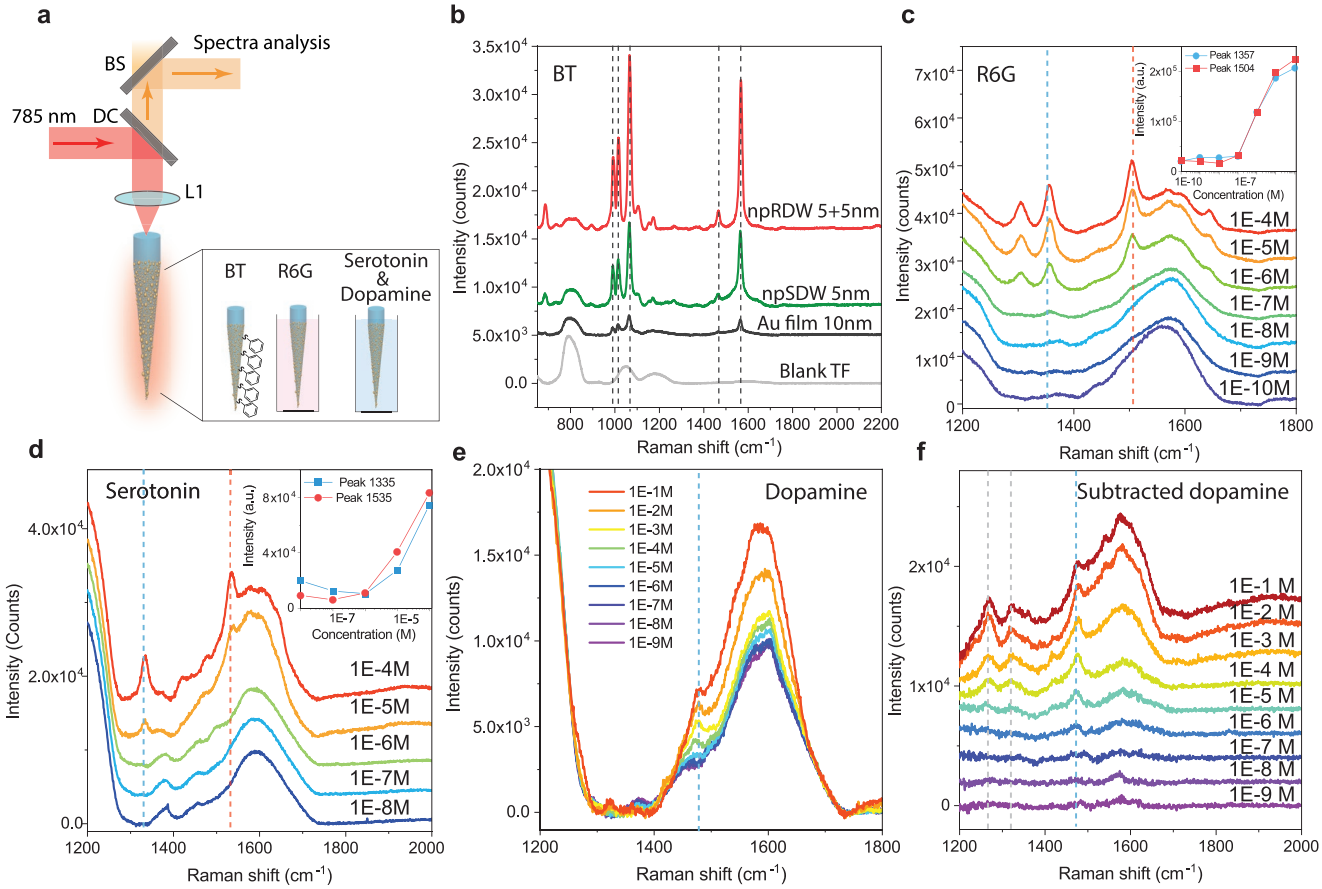

Figure 4. a) Schematic configuration for NIs-TFs through measurements with BT molecule functionalization, R6G, and neurotransmitters (dopamine and serotonin) aqueous solutions. b) SERS response of BT molecule functionalized npRDW (red curve), npSDW (green curve), 10 nm gold film coated (black curve) and blank (gray curve) TFs, the dashed vertical lines indicate the molecular signature peaks at 992, 1015, 1065, 1465 and 1567 cm^{-1}. c) npRDW TF detection of R6G aqueous solutions with concentrations varying from 10^{-10} to 10^{-4} M (the solid curves from bottom to top); the spectra were offset vertically for easier visualization. The inset shows the concentration dependence of the area under 1356 (blue points) and 1504 cm^{-1} (red points) after locally subtracting the background. d) npRDW TF detection of serotonin aqueous solution with concentrations varying from 10^{-8} to 10^{-4} M (the solid curves from bottom to top), the spectra were offset vertically for easier visualization. The inset shows the concentration dependence of the area under 1335 (blue points) and 1535 cm^{-1} (red points) after locally subtracting the background. e) npRDW TF detection of dopamine aqueous solution with concentrations varying from 10^{-9} to 10^{-1} M (the solid curves), the blue vertical dashed line indicates the dopamine peak at 1476 cm^{-1}. f) The dopamine SERS spectra in (e) with silica background subtracted.

(serotonin and dopamine). As in the case of BT, the molecular SERS dominates the overall spectra, and silica Raman becomes a negligible background. With the decrease of the relative strengths on the molecular SERS in the examples of R6G and neurotransmitters, the molecular fingerprints overlap with silica Raman background. The relative strength of R6G SERS is slightly stronger than the two neurotransmitters, as it gives a lower LOD. Serotonin and dopamine SERS are at the same level of relative strength, resulting in the same LOD.

2. Discussion and Conclusion

We proposed a novel approach to exploit in-situ nucleation of gold NIs on the nonplanar surface of TFs, and to establish a technological platform to bring nanophotonic structures into the brain, with the aim of implementing label-free SERS detection within. Previously, two works have shown that colloidal metal nanoparticles deposited onto nanofiber tips can function as nanosensors to enhance neurotransmitters' signal in the vicinity of neuron cells, but with excitation and collection occurring from outside of the fiber.[42,43] TFs coated with silver-doped PVA have also proven to detect dopamine SERS signal at 10^{-3} M in the visible region.[49] Overall, the optimization of the device performance is a crucial aspect for neuroscience community moving toward in vivo studies, as physiological sensitivity is required in the through-fiber measurements. With the aim of simultaneously optimizing excitation yield, collection of scattered photons and NIR spectral coverage, we developed the npRDW strategy, which generates a monolayer of densely packed gold NIs with narrow plasmonic gaps (<10 nm) uniformly distributed on the entire optically active surface of the TFs. The plasmonic resonances can be excited with a wide range of polarizations and wavevector components supported by the fiber. In this way, the fraction of excitation power that results in field enhancement is

maximized. Efficient collection was instead obtained by the ultrathin homogeneous NIs monolayer, that covers the full taper extent despite its nonplanar surface with nonconstant radius of curvature. This maximizes the overlap between the field enhancement in the nanogaps and the maximum region of light collection of the taper, therefore, the collection of resonantly scattered signal is maximized. NIR spectral coverage for both excitation and scattering wavelengths reduces the influence of the tissue background. This led us to obtain a plasmonic probe for SERS detection of neurotransmitters down to a concentration of 10^{-5} M working in the NIR range, with both excitation and scattered photons guided in the same waveguide.

The detection capability of our device is compatible with higher level of physiological concentrations, which has been reported in the range of nanomolar to tens of micromolar in the mouse brain.[16,52–54,62,63] To name a few examples, Patriarchi et al.[16] have estimated a dopamine release in the range of 1 to 3×10^{-5} M by correlating DLight response ($\Delta F/F$) to the concentration–response curves obtained in titration experiments, and Beyene et al.[52] also showed dopamine concentration in brain tissue arising from the activity of a single dopaminergic terminal can exceed concentrations of 1×10^{-6} M from the release site in a distance dependent manner. For serotonin, fast-scan cyclic voltammetry approach has shown that extra synaptic concentration can reach low micromolar range.[53,54] It is worth to note that achieving label-free detection of neurotransmitters has remarkable translational potential not only with respect to the mouse animal model, but also in larger models such as nonhuman primates (NHPs), which will likely entice higher concentrations of neurotransmitters.[64] Therefore, the NIs-TFs show a promising sensing capability to identify neurotransmitter at physiological conditions.

Nevertheless, further steps are required to move this technology toward animal models. These steps include: i) understanding whether the mechanical interaction between the brain tissue and the probe will introduce severe damages, since the tissue is intrinsically different from liquid phase environments, where nanoparticle-based SERS probes can be applied;[65–67] ii) testing the potential toxicity due to gold ions or NIs release from the fiber surface; iii) boosting the temporal response of the approach; and iv) developing a method to discriminate across multiple chemical compounds, for example using barcoding data processing[43] or to functionalize the structured fiber probes to be able to catch the target analyte.[68,69]

In this view, we believe that the SERS-active TFs neural probes have the potential to complement existing methods to detect neurotransmitters, currently employing GEI or cyclic voltammetry.[70,71] Additionally, we are confident that our npRDW approach can envisage further experimental applications such as: i) plasmonic heating in the brain tissue as in cancer therapy,[72–74] or for thermally triggering neural activity;[75] ii) combining with the dynamic optical element for holographic SERS endoscopic imaging;[76] iii) perspective applications on the study of neurotransmitters' crosstalk between nerves across the central nervous system and peripheral tissues;[77] and iv) on-chip absorption overtone spectroscopy,[78–80] where the plasmonic enhancement can be used to facilitate the weak overtone transitions.

3. Experimental Section

NIs Functionalized SERS Fiber Probe Fabrication: The standard multimode silica optical fibers (Thorlabs, FG050LGA, 0.22 NA, Low-OH, Ø50 µm Core and FG200LEA, 0.22 NA, Low-OH, Ø200 µm Core) were used for flat fibers (FFs) and TFs fabrication. As a preparation step, all the fibers were put in an acetone bath for 30 min to remove the acrylate jacket. For the FFs, the fibers were cut with a fixed length of 7.5 cm. Then, a manual fiber cleaver (Thorlabs, XL411) was used to cut one side of the fiber to obtain a smooth top flat fiber facet. For the TFs, the fibers were cut with a fixed length of 12 cm to fit the puller system (Sutter P-2000), then TFs were pulled rapidly, after laser heating, with very small taper angles.[81] During the evaporation process, the FFs were fixed on a batch mount printed with the 3D printer (Ultimaker S3) to align the top surfaces of fibers normal to the gold source in a crucible of an e-beam evaporator (Thermionics laboratory, Inc. e-GunTM). TFs were mounted on a rotational motor to ensure conformal gold evaporation over the entire TFs surfaces. For all evaporations, the evaporation rate was kept the same as 0.2 Å s^{-1}, with chamber pressure $<6 \times 10^{-6}$ mbar. The thickness control for evaporation on TFs was linked to flat surfaces evaporation with relation $T_{TFs} = 1/\pi \times T_{FFs}$, thus, for npRDW TFs, the actual gold film thickness of twice evaporation were controlled as $t_1 + t_2 = 15 + 15$ nm. When the evaporation procedure finished, the fibers were detached from the mount and arranged in a ceramic bowl without any adhesive for thermal annealing in a muffle furnace (Nabertherm B180). The furnace was controlled to gradually ramp up the temperature from room temperature (RT) to 600 °C with a rate of 10 °C min^{-1}, and held at 600 °C for 1 h, then allowed to cool in ambient to RT. Eventually, the nonstructured side of fabricated fibers was connected to metallic ferrules with a diameter of 1.25 mm, and went through the same manual polishing process to ensure stability during the optical characterizations.

In the fabrication process, the initial film deposition was crucial for the final NIs morphology, and the initial film status (the nominal film thickness and the structure of the voids at the metal–ambient and metal–glass interfaces) was the main parameter contributing to the final NIs' size and distribution variations. Thus, plasmonic fiber fabricated within the same batch show stable appearance. As displayed in Figure S2.1a–c, Supporting Information, LOD experiments for three different fibers (randomly selected within the same batch) with nominally identic fabrication parameters, show stable optical response.

Extinction Spectra Measurement: The extinction spectra were measured with a transmission configuration using a home-built microscope; the schematic illustration of the setup can be found in Figure S5.1, Supporting Information. Briefly, a halogen lamp with a SMA connector was used to excite the fiber through a fiber patch-cord connection, which delivered the broadband light through the NIs functionalized fiber facet. The transmitted light was collected with a 4× objective (Olympus XLFluor 4x/340, NA = 0.28), and then directed to a spectrometer (Horiba iHR320) with an achromatic doublet (Ø25.4 mm, f = 100 mm). The spectrometer was equipped with a 300 lp/mm grating and synapse EMCCD for the spectra acquisition. To subtract the actual extinction spectrum of NIs-FF (Ext_{NIs}), the transmission spectrum of NIs-FF (T_{NIs}) was corrected by a blank FF transmission spectrum (T_{blank}) with relation ($Ext_{NIs} = (T_{blank} - T_{NIs})/T_{blank}$), to exclude the systematic response.

BT Molecule Functionalization: Benzenethiol (BT, C_6H_5SH) molecules were purchased from Sigma-Aldrich (99%). The fabricated NIs fiber facet along with reference fibers were immersed in BT molecule methanol solution (6 mM) for 6.5 h, then the fibers were rinsed by stirring them in a cup of clean methanol solution for 10 min. The rinsing process was repeated three times with a clean methanol solution each time to ensure a successful monolayer functionalization.

Raman Measurements with 633 nm Excitation: The NIs annealed tip of the flat fiber acted as a flat substrate for SERS measurements and was placed perpendicularly to the objective. The detailed optical setup can be found in Figure S5.2, Supporting Information; in short, the collimated laser beam fully filled the back aperture of the objective

(40×, 0.65 NA, AMEP4625, ThermoFisher), resulting in a light spot of 1.5 µm. The back-scattered Raman signal was collected through the same objective and transmitted by a long-pass dichroic mirror (DC, Semrock, LPD02-633RU) toward the spectrometer. A notch filter (NF, Semrock, NF03-633E-25) was used to remove the residual laser excitation and the resulting signal was focused onto a round to linear fiber bundle using a lens (f = 50 mm). The linear facet of the bundle was imaged on the entrance slit of a spectrometer (iHR320, Horiba). The Raman measurements were performed with slits at 200 µm and a grating of 600 l mm^{-1} (blaze 750 nm). Spectra were recorded on a SYNAPSE CCD cooled to −50 °C with 30 s acquisition time and 1 mW excitation power. The raw spectra were treated with baseline correction (ALS). Since the excitation spot was much smaller than the fiber core (Ø50 µm), eight spectra were acquired at different positions for one sample, and the final spectrum was the average spectrum of the eight times measurements.

Raman Measurements with 785 nm Excitation: The optical setup for the home-built Raman microscope is shown in Figure S5.3, Supporting Information. Briefly, the collimated Laser beam fully filled the back aperture of the focus lens L1 (aspheric, Ø25.0 mm, f = 20 mm), resulting in a light spot of 200 µm in diameter. The Raman signal was separated from the pump laser using a dichroic mirror (DC: Semrock, LPD02-785RU-25) and a long-pass razor-edge filter (F1: Semrock, LP02-785RU-25). The signal was then routed to a spectrometer (Horiba iHR320). The Raman measurements were performed with a slit at 200 µm and a 600 l mm^{-1} (blaze 750 nm) grating. Spectra were recorded on a SYNAPSE CCD cooled to −50 °C. All the raw spectra were treated with baseline correction (ALS). Two different measurements were based on this setup, list as follows: i) SERS measurements on flat substrates. After 633 nm measurements, the same set of FFs was configured with the facet facing the focus lens. The laser spot fully covered the whole fiber facet, and the spectra were taken with 77.7 mW laser power and 5 s exposure time; and ii) through-TFs SERS measurements. The fibers were configured with the distal end facing the focus lens, the laser was injected over the full angular acceptance of the fiber (NA 0.22) to recruit most of the propagating modes. The signal, collected by the taper, was then routed to a spectrometer for spectra analysis. For different molecules, the measurement parameters including laser power and exposure time were listed as follows: BT molecules (24 mW, 5 s), R6G (68 mW, 30 s), serotonin, and dopamine (68 mW, 60 s). R6G (Rhodamine 6G, $C_{28}H_{31}N_2O_3Cl$), dopamine (3-hydroxytyramine hydrochloride, $C_8H_{12}ClNO_2$), and serotonin (5-hydroxytryptamine, $C_{10}H_{12}N_2O$) were all purchased from Merck KGaA.

Statistical Analysis of NIs Morphology: For the statistical analysis, high-quality SEM images were acquired with the FEI Helios Nanolab 600i Dual Beam system. The SEM image acquisitions were conducted after sputtering a thin layer of gold on all the NIs surface to provide sufficient conductivity. On the TFs, the large curvature near the taper tip results in a tilted image and less contrast between NIs and the background, making the statistical analysis difficult when L < 50 µm. The ImageJ software was used for the morphology analysis. The areas of physical occupation (S) of each NIs were extracted from the binary formats of each SEM image, along with the overall coverage rate (C). The diameters of each NIs were obtained by assuming NIs as circular, thus $D = 2\times\sqrt{S/\pi}$. For the effective gap (g_{eff}) size evaluation, all the NIs were assumed to be the average size, occupying unit cells with an occupation rate of coverage rate (circular and one-modal periodic approximations), thus $g_{eff} = \sqrt{S_{Aver}/C} - 2\times\sqrt{S_{Aver}/\pi}$, where S_{Aver} is the average area of all the extracted NIs areas.

It is worth noting that the bimodal distribution of RDW morphologies induce wider NIs size distribution, the above g_{eff} evaluation method that depends on circular and one-modal periodic approximations could be less representative. Thus, a more generalized computational method to analyze the effective gap size of the RDW bimodal distribution morphologies, which relies on finding the minimal distances for each NIs to its' nearest neighbor through point-to-point computation using NIs' boundaries, was developed. The detailed analysis shows the generalized computational method gives a slightly smaller value of effective gaps size, and the gap distribution appears stable along the curved taper surface under both analysis approaches (Figure S3.3, Supporting Information). The detailed comparison is included in Section S3 in the Supporting Information, and the analysis program is available on reasonable request.

Electromagnetic Simulations: The results in Figure 3e–h have been obtained by simulating 3D time-harmonic Maxwell's equations using COMSOL Multiphysics, a commercially available software based on the finite element method. To emphasize the effect of the interparticle distances and reduce the computational cost a periodic system characterized by a hexagonal lattice in which a larger gold disk was surrounded by smaller ones was considered. In order to mimic the droplet-like shape of the fabricated sample, the top edge of the disk was rounded with a radius of curvature r = 6 nm. The particle sits on an infinite dielectric substrate with a refractive index n = 1.4. Optical constants of gold were obtained from Ref. [82]. The mesh resolution was chosen so that transmittance results were converged to <0.1% at resonance. The unpolarized field map distribution has been obtained by summing up the local fields obtained by exciting the array with a vertically and horizontally polarized plane wave impinging at normal incidence as $|E_{unpol}| = (|E_h| + |E_v|)/2$, as shown in Figure 3e,f. The average field enhancements were obtained by averaging the field maps. The transmittances of the systems were used to compare with the experimental extinction spectra as they were measured in a transmission configuration.

Supporting Information

Supporting Information is available from the Wiley Online Library or from the author.

Acknowledgements

M.D.V. and Fe.P. contributed equally to this work and are co-last-authors. D.Z., Li.C., R.M.-B., A.B., C.C., F.T., F.D.A., L.M.P., M.V., M.D.V., and Fe.P. acknowledge funding from the European Union's Horizon 2020 Research and Innovation Program under Grant Agreement No. 828972. Fi.P., A.B., B.S., and Fe.P. acknowledge funding from the European Research Council under the European Union's Horizon 2020 Research and Innovation Program under Grant Agreement No. 677683. Lu.C. acknowledges financial support by the Italian Ministry of Economic Development through the Project "GENESI"-Development of innovative radiopharmaceuticals and biomarkers for the diagnosis of tumors of the male and female reproductive apparatus (cod. F/180003/01-03/X43, Call MISE "Intelligent Factory, Agri food and Life Sciences"). Fi.P., M.D.V., and Fe.P. acknowledge that this project has received funding from the European Union's Horizon 2020 Research and Innovation Program under Grant Agreement No. 101016787. M.P., Fe.P., and M.D.V. were funded by the U.S. National Institutes of Health (Grant No. 1UF1NS108177-01).

Conflict of Interest

M.D.V. and Fe.P. are founders and hold private equity in Optogenix, a company that develops, produces, and sells technologies to deliver light into the brain.

Data Availability Statement

The data that support the findings of this study are available from the corresponding author upon reasonable request.

Keywords

gold nanoislands, gold-nanoparticles-decorated tapered fibers, label-free detection, neurotransmitters, plasmonics, solid-state dewetting, tapered fibers

Received: January 27, 2022
Revised: October 21, 2022
Published online:

[1] E. S. Boyden, F. Zhang, E. Bamberg, G. Nagel, K. Deisseroth, *Nat. Neurosci.* **2005**, *8*, 1263.
[2] K. Deisseroth, *Nat. Methods* **2011**, *8*, 26.
[3] O. Yizhar, L. E. Fenno, T. J. Davidson, M. Mogri, K. Deisseroth, *Neuron* **2011**, *71*, 9.
[4] L. Fenno, O. Yizhar, K. Deisseroth, *Annu. Rev. Neurosci.* **2011**, *34*, 389.
[5] A. M. Aravanis, L.-P. Wang, F. Zhang, L. A. Meltzer, M. Z. Mogri, M. B. Schneider, K. Deisseroth, *J. Neural Eng.* **2007**, *4*, S143.
[6] A. R. Adamantidis, F. Zhang, A. M. Aravanis, K. Deisseroth, L. de Lecea, *Nature* **2007**, *450*, 420.
[7] H. Dana, Y. Sun, B. Mohar, B. K. Hulse, A. M. Kerlin, J. P. Hasseman, G. Tsegaye, A. Tsang, A. Wong, R. Patel, J. J. Macklin, Y. Chen, A. Konnerth, V. Jayaraman, L. L. Looger, E. R. Schreiter, K. Svoboda, D. S. Kim, *Nat. Methods* **2019**, *16*, 649.
[8] L. Tian, S. A. Hires, T. Mao, D. Huber, M. E. Chiappe, S. H. Chalasani, L. Petreanu, J. Akerboom, S. A. McKinney, E. R. Schreiter, C. I. Bargmann, V. Jayaraman, K. Svoboda, L. L. Looger, *Nat. Methods* **2009**, *6*, 875.
[9] J. Akerboom, T.-W. Chen, T. J. Wardill, L. Tian, J. S. Marvin, S. Mutlu, N. C. Calderón, F. Esposti, B. G. Borghuis, X. R. Sun, A. Gordus, M. B. Orger, R. Portugues, F. Engert, J. J. Macklin, A. Filosa, A. Aggarwal, R. A. Kerr, R. Takagi, S. Kracun, E. Shigetomi, B. S. Khakh, H. Baier, L. Lagnado, S. S.-H. Wang, C. I. Bargmann, B. E. Kimmel, V. Jayaraman, K. Svoboda, D. S. Kim, et al., *J. Neurosci.* **2012**, *32*, 13819.
[10] J. S. Marvin, B. G. Borghuis, L. Tian, J. Cichon, M. T. Harnett, J. Akerboom, A. Gordus, S. L. Renninger, T.-W. Chen, C. I. Bargmann, M. B. Orger, E. R. Schreiter, J. B. Demb, W.-B. Gan, S. A. Hires, L. L. Looger, *Nat. Methods* **2013**, *10*, 162.
[11] J. Wu, A. S. Abdelfattah, H. Zhou, A. Ruangkittisakul, Y. Qian, K. Ballanyi, R. E. Campbell, *ACS Chem. Biol.* **2018**, *13*, 1832.
[12] J. S. Marvin, B. Scholl, D. E. Wilson, K. Podgorski, A. Kazemipour, J. A. Müller, S. Schoch, F. J. U. Quiroz, N. Rebola, H. Bao, J. P. Little, A. N. Tkachuk, E. Cai, A. W. Hantman, S. S.-H. Wang, V. J. DePiero, B. G. Borghuis, E. R. Chapman, D. Dietrich, D. A. DiGregorio, D. Fitzpatrick, L. L. Looger, *Nat. Methods* **2018**, *15*, 936.
[13] N. Helassa, C. D. Dürst, C. Coates, S. Kerruth, U. Arif, C. Schulze, J. S. Wiegert, M. Geeves, T. G. Oertner, K. Török, *Proc. Natl. Acad. Sci. USA* **2018**, *115*, 5594.
[14] J. S. Marvin, Y. Shimoda, V. Magloire, M. Leite, T. Kawashima, T. P. Jensen, I. Kolb, E. L. Knott, O. Novak, K. Podgorski, N. J. Leidenheimer, D. A. Rusakov, M. B. Ahrens, D. M. Kullmann, L. L. Looger, *Nat. Methods* **2019**, *16*, 763.
[15] J. Wan, W. Peng, X. Li, T. Qian, K. Song, J. Zeng, F. Deng, S. Hao, J. Feng, P. Zhang, Y. Zhang, J. Zou, S. Pan, M. Shin, B. J. Venton, J. J. Zhu, M. Jing, M. Xu, Y. Li, *Nat. Neurosci.* **2021**, *24*, 746.
[16] T. Patriarchi, J. R. Cho, K. Merten, M. W. Howe, A. Marley, W.-H. Xiong, R. W. Folk, G. J. Broussard, R. Liang, M. J. Jang, H. Zhong, D. Dombeck, M. von Zastrow, A. Nimmerjahn, V. Gradinaru, J. T. Williams, L. Tian, *Science* **2018**, *360*, eaat4422.
[17] F. Sun, J. Zeng, M. Jing, J. Zhou, J. Feng, S. F. Owen, Y. Luo, F. Li, H. Wang, T. Yamaguchi, Z. Yong, Y. Gao, W. Peng, L. Wang, S. Zhang, J. Du, D. Lin, M. Xu, A. C. Kreitzer, G. Cui, Y. Li, *Cell* **2018**, *174*, 481.
[18] M. Jing, P. Zhang, G. Wang, J. Feng, L. Mesik, J. Zeng, H. Jiang, S. Wang, J. C. Looby, N. A. Guagliardo, L. W. Langma, J. Lu, Y. Zuo, D. A. Talmage, L. W. Role, P. Q. Barrett, L. I. Zhang, M. Luo, Y. Song, J. J. Zhu, Y. Li, *Nat. Biotechnol.* **2018**, *36*, 726.
[19] J. Feng, C. Zhang, J. E. Lischinsky, M. Jing, J. Zhou, H. Wang, Y. Zhang, A. Dong, Z. Wu, H. Wu, W. Chen, P. Zhang, J. Zou, S. A. Hires, J. J. Zhu, G. Cui, D. Lin, J. Du, Y. Li, *Neuron* **2019**, *102*, 745.
[20] K. Zheng, T. P. Jensen, L. P. Savtchenko, J. A. Levitt, K. Suhling, D. A. Rusakov, *Sci. Rep.* **2017**, *7*, 42022.
[21] S. H. Lee, C. Jin, E. Cai, P. Ge, Y. Ishitsuka, K. W. Teng, A. A. de Thomaz, D. Nall, M. Baday, O. Jeyifous, D. Demonte, C. M. Dundas, S. Park, J. Y. Delgado, W. N. Green, P. R. Selvin, *eLife* **2017**, *6*, e27744.
[22] Y. Sych, M. Chernysheva, L. T. Sumanovski, F. Helmchen, *Nat. Methods* **2019**, *16*, 553.
[23] H. Adelsberger, C. Grienberger, A. Stroh, A. Konnerth, Cold Spring Harbor Protoc **2014**, http://cshprotocols.cshlp.org/content/2014/10/pdb.prot084145.full.pdf+html.
[24] E. Martianova, S. Aronson, C. D. Proulx, *J. Visualized Exp.* **2019**, 60278.
[25] L. Lu, P. Gutruf, L. Xia, D. L. Bhatti, X. Wang, A. Vazquez-Guardado, X. Ning, X. Shen, T. Sang, R. Ma, G. Pakeltis, G. Sobczak, H. Zhang, D. Seo, M. Xue, L. Yin, D. Chanda, X. Sheng, M. R. Bruchas, J. A. Rogers, *Proc. Natl. Acad. Sci. USA* **2018**, *115*, E1374.
[26] M. Z. Lin, M. J. Schnitzer, *Nat. Neurosci.* **2016**, *19*, 1142.
[27] L. Opilik, T. Schmid, R. Zenobi, *Annu. Rev. Anal. Chem.* **2013**, *6*, 379.
[28] Z. Wu, D. Lin, Y. Li, *Nat. Rev. Neurosci.* **2022**, *23*, 257.
[29] Y. Da, S. Luo, Y. Tian, *ACS Appl. Mater. Interfaces* **2023**, *15*, 138.
[30] S. Nie, S. R. Emory, *Science* **1997**, *275*, 1102.
[31] K. Kneipp, Y. Wang, H. Kneipp, L. T. Perelman, I. Itzkan, R. R. Dasari, M. S. Feld, *Phys. Rev. Lett.* **1997**, *78*, 1667.
[32] H. Xu, E. J. Bjerneld, M. Käll, L. Börjesson, *Phys. Rev. Lett.* **1999**, *83*, 4357.
[33] H. Adelsberger, O. Garaschuk, A. Konnerth, *Nat. Neurosci.* **2005**, *8*, 988.
[34] J. Muir, Z. S. Lorsch, C. Ramakrishnan, K. Deisseroth, E. J. Nestler, E. S. Calipari, R. C. Bagot, *Neuropsychopharmacology* **2018**, *43*, 255.
[35] F. Pisanello, L. Sileo, I. A. Oldenburg, M. Pisanello, L. Martiradonna, J. A. Assad, B. L. Sabatini, M. De Vittorio, *Neuron* **2014**, *82*, 1245.
[36] F. Pisanello, G. Mandelbaum, M. Pisanello, I. A. Oldenburg, L. Sileo, J. E. Markowitz, R. E. Peterson, A. D. Patria, T. M. Haynes, M. S. Emara, B. Spagnolo, S. R. Datta, M. De Vittorio, B. L. Sabatini, *Nat. Neurosci.* **2017**, *20*, 1180.
[37] B. Spagnolo, A. Balena, R. T. Peixoto, M. Pisanello, L. Sileo, M. Bianco, A. Rizzo, F. Pisano, A. Qualtieri, D. D. Lofrumento, F. De Nuccio, J. A. Assad, B. L. Sabatini, M. De Vittorio, F. Pisanello, *Nat. Mater.* **2022**, *21*, 826.
[38] F. Pisano, M. Pisanello, S. J. Lee, J. Lee, E. Maglie, A. Balena, L. Sileo, B. Spagnolo, M. Bianco, M. Hyun, M. De Vittorio, B. L. Sabatini, F. Pisanello, *Nat. Methods* **2019**, *16*, 1185.
[39] F. Pisano, M. F. Kashif, A. Balena, M. Pisanello, F. De Angelis, L. M. de la Prida, M. Valiente, A. D'Orazio, M. De Vittorio, M. Grande, F. Pisanello, *Adv. Opt. Mater.* **2022**, *10*, 2101649.
[40] F. Pisano, A. Balena, M. F. Kashif, M. Pisanello, G. de Marzo, L. Algieri, A. Qualtieri, L. Sileo, T. Stomeo, A. D'Orazio, M. D. Vittorio, F. Pisanello, M. Grande, *Nanotechnology* **2020**, *31*, 435301.
[41] J. Cao, D. Zhao, Q. Mao, *Analyst* **2017**, *142*, 596.
[42] H. Zhu, F. Lussier, C. Ducrot, M.-J. Bourque, J. P. Spatz, W. Cui, L. Yu, W. Peng, L.-É. Trudeau, C. G. Bazuin, J.-F. Masson, *ACS Appl. Mater. Interfaces* **2019**, *11*, 4373.
[43] F. Lussier, T. Brulé, M.-J. Bourque, C. Ducrot, L.-É. Trudeau, J.-F. Masson, *Faraday Discuss.* **2017**, *205*, 387.

[44] Z. Chen, Z. Dai, N. Chen, S. Liu, F. Pang, B. Lu, T. Wang, *IEEE Photonics Technol. Lett.* **2014**, *26*, 777.
[45] J. Cao, D. Zhao, Q. Mao, *RSC Adv.* **2015**, *5*, 99491.
[46] J. Cao, D. Zhao, Y. Qin, *Talanta* **2019**, *194*, 895.
[47] T. Li, Z. Yu, Z. Wang, Y. Zhu, J. Zhang, *Sensors* **2021**, *21*, 2300.
[48] W. Xu, Z. Chen, N. Chen, H. Zhang, S. Liu, X. Hu, J. Wen, T. Wang, *Sensors* **2017**, *17*, 467.
[49] M. Volkan, D. L. Stokes, T. Vo-Dinh, *Appl. Spectrosc.* **2000**, *54*, 1842.
[50] J. Zhang, S. Chen, T. Gong, X. Zhang, Y. Zhu, *Plasmonics* **2016**, *11*, 743.
[51] H. Zhu, J.-F. Masson, C. G. Bazuin, *ACS Appl. Nano Mater.* **2020**, *3*, 516.
[52] A. G. Beyene, I. R. McFarlane, R. L. Pinals, M. P. Landry, *ACS Chem. Neurosci.* **2017**, *8*, 2275.
[53] M. A. Bunin, R. M. Wightman, *J. Neurosci.* **1998**, *18*, 4854.
[54] M. A. Bunin, C. Prioleau, R. B. Mailman, R. M. Wightman, *J. Neurochem.* **1998**, *70*, 1077.
[55] M. Pisanello, F. Pisano, L. Sileo, E. Maglie, E. Bellistri, B. Spagnolo, G. Mandelbaum, B. L. Sabatini, M. De Vittorio, F. Pisanello, *Sci. Rep.* **2018**, *8*, 4467.
[56] D. G. Moore, H. R. Thornton, *J. Res. Natl. Bur. Stand.* **1959**, *62*, 127.
[57] D. M. Mattox, *J. Appl. Phys.* **1966**, *37*, 3613.
[58] L.-J. Wan, M. Terashima, H. Noda, M. Osawa, *J. Phys. Chem. B* **2000**, *104*, 3563.
[59] C. M. Whelan, M. R. Smyth, C. J. Barnes, *Langmuir* **1999**, *15*, 116.
[60] J. Frangioni, *Curr. Opin. Chem. Biol.* **2003**, *7*, 626.
[61] G. Hong, A. L. Antaris, H. Dai, *Nat. Biomed. Eng.* **2017**, *1*, 0010.
[62] L. H. Parsons, J. B. Justice, *J. Neurochem.* **1992**, *58*, 212.
[63] A. Abdalla, C. W. Atcherley, P. Pathirathna, S. Samaranayake, B. Qiang, E. Peña, S. L. Morgan, M. L. Heien, P. Hashemi, *Anal. Chem.* **2017**, *89*, 9703.
[64] P. J. Fitzgerald, *Neurosci. Biobehav. Rev.* **2009**, *33*, 1037.
[65] S. Liu, M. Rong, H. Zhang, N. Chen, F. Pang, Z. Chen, T. Wang, J. Yan, *Biomed. Opt. Express* **2016**, *7*, 810.
[66] X. Fu, Z. Wang, J. Li, S. Ma, G. Fu, W. Jin, W. Bi, Y. Dong, *IEEE Photonics J.* **2021**, *13*, 6800513.
[67] J. Kwak, W. Lee, J.-B. Kim, S.-I. Bae, K.-H. Jeong, *J. Biomed. Opt.* **2019**, *24*, 037001.
[68] A. Vázquez-Guardado, S. Barkam, M. Peppler, A. Biswas, W. Dennis, S. Das, S. Seal, D. Chanda, *Nano Lett.* **2019**, *19*, 449.
[69] C.-X. Shi, Z.-P. Chen, Y. Chen, Q. Liu, R.-Q. Yu, *Chemom. Intell. Lab. Syst.* **2017**, *169*, 87.
[70] J. T. Yorgason, D. M. Zeppenfeld, J. T. Williams, *J. Neurosci.* **2017**, *37*, 2086.
[71] N. A. Courtney, C. P. Ford, *J. Neurosci.* **2014**, *34*, 7645.
[72] D. K. Chatterjee, P. Diagaradjane, S. Krishnan, *Ther. Delivery* **2011**, *2*, 1001.
[73] G. Baffou, R. Quidant, *Laser Photonics Rev.* **2013**, *7*, 171.
[74] J. Ribera, C. Vilches, V. Sanz, I. de Miguel, I. Portolés, B. Córdoba-Jover, E. Prat, V. Nunes, W. Jiménez, R. Quidant, M. Morales-Ruiz, *ACS Nano* **2021**, *15*, 7547.
[75] J. W. Lee, H. Jung, H. H. Cho, J. H. Lee, Y. Nam, *Biomaterials* **2018**, *153*, 59.
[76] L. Collard, F. Pisano, D. Zheng, A. Balena, M. F. Kashif, M. Pisanello, A. D'Orazio, L. M. de la Prida, C. Ciracì, M. Grande, M. De Vittorio, F. Pisanello, *Small* **2022**, *18*, 2200975.
[77] M. Monje, J. C. Borniger, N. D'Silva, B. Deneen, P. B. Dirks, F. Fattahi, P. S. Frenette, L. Garzia, D. H. Gutmann, D. Hanahan, S. L. Hervey-Jumper, H. Hondermarck, J. B. Hurov, A. Kepecs, S. M. Knox, A. C. Lloyd, C. Magnon, J. L. Saloman, R. A. Segal, E. K. Sloan, X. Sun, M. D. Taylor, K. J. Tracey, L. C. Trotman, D. A. Tuveson, T. C. Wang, R. A. White, F. Winkler, *Cell* **2020**, *181*, 219.
[78] A. Karabchevsky, A. Katiyi, A. S. Ang, A. Hazan, *Nanophotonics* **2020**, *9*, 3733.
[79] A. Katiyi, A. Karabchevsky, *J. Lightwave Technol.* **2017**, *35*, 2902.
[80] A. Karabchevsky, A. Katiyi, M. I. M. Bin Abdul Khudus, A. V. Kavokin, *ACS Photonics* **2018**, *5*, 2200.
[81] L. Sileo, M. Pisanello, M. De Vittorio, F. Pisanello, *Proc. SPIE* **2015**, *9305*, 93052O.
[82] R. L. Olmon, B. Slovick, T. W. Johnson, D. Shelton, S.-H. Oh, G. D. Boreman, M. B. Raschke, *Phys. Rev. B* **2012**, *86*, 235147.